Research Square

Preprints are preliminary reports that have not undergone peer review.
They should not be considered conclusive, used to inform clinical practice,
or referenced by the media as validated information.

Structural, Morphological, Optical and Photocatalytic Properties of ZnO50%-CdO50% Mixed-Oxide Nanoparticles

Vikas Patil

vikasgpatil8@gmail.com

Yashwantrao Chavan Maharashtra Open University

Vinod Barote

Sant Dnyaneshwar Mahavidyalaya, Soegaon

Santosh Katariya

SIES College Of Arts, Science and Commerce, (Autonomous), Sion

Umesh Maske

K. J. Somaiya Polytechnic

Sunanda Patil

K.T.H.M. College

Dhananjay Mane

Yashwantrao Chavan Maharashtra Open University

Research Article

Keywords: ZnO-CdO nanoparticles, heterojunction photocatalysis, sonochemical synthesis, advanced oxidation processes, dye degradation, lemon extract capping, mixed-oxide semiconductors, water treatment

Posted Date: April 18th, 2026

DOI: https://doi.org/10.21203/rs.3.rs-8510716/v1

License: This work is licensed under a Creative Commons Attribution 4.0 International License.
Read Full License

Additional Declarations: No competing interests reported.

Structural, Morphological, Optical and Photocatalytic Properties of $ZnO_{50\%}$-$CdO_{50\%}$ Mixed-Oxide Nanoparticles

Vikas G. Patil[ab], Vinod K. Barote[c], Santosh B Katariya[d], Umesh A Maske[e], Sunanda V Patil[f], Dhananjay V. Mane[g,h]

[a]Research Scholor, School of Sciences, YCMOU Nashik 420003 India

[b]Department of Sciences, K. J. Somaiya Polytechnic Mumbai 400077 India

[c]Department of Physics, Sant Dnyaneshwar Mahavidyalaya, Soegaon, Chhatrapati Sambhajinagar 431001 India

[d]Department of Chemistry, SIES College Of Arts, Science and Commerce, (Autonomous), Sion, Mumbai 400022 India

[e]K. J. Somaiya Polytechnic Mumbai 400077 India

[f]Ex Student, K.T.H.M. College Nashik 420003 India

[g]Former. Regional Director, YCMOU Nashik 420003 India

[h]Department of Chemistry, Shri Chhatrapati Shivaji College Omerga, Dharashiv 413606 India

Corresponding author's email: vikasgpatil8@gmail.com

Abstract

This investigation explores the synthesis, comprehensive characterization, and photocatalytic performance of equimolar $ZnO_{50\%}$-$CdO_{50\%}$ mixed-oxide nanoparticles prepared via sonochemical methodology with and without lemon extract capping. Structural analysis through X-ray diffraction revealed hexagonal wurtzite architecture with lattice parameters a = 3.861 Å and c = 5.220 Å for uncapped samples, indicating significant lattice distortion from Cd^{2+} incorporation. Morphological investigations using scanning electron microscopy and high-resolution transmission electron microscopy demonstrated average particle sizes of 62 nm and 48 nm respectively, with mixed cubic-spherical geometries evidencing solid solution formation. Lemon-capped nanoparticles exhibited reduced crystallite dimensions (17.03 nm) with enhanced dispersion and morphological uniformity. Optical characterization revealed band gap values approximating 2.8-3.0 eV, representing intermediate properties between constituent oxides. Photocatalytic evaluation against three organic pollutants demonstrated exceptional performance: 91.98% degradation efficiency for Methylene Blue, 88.27% for Crystal Violet, and 47.45% for tetrazine under UV irradiation over 165 minutes. The equimolar composition maximized heterojunction interface area, optimizing charge separation and reactive oxygen species generation. Lemon capping significantly enhanced catalytic activity through surface passivation and improved dispersion. These findings establish $ZnO_{50\%}$-$CdO_{50\%}$ nanocomposites as promising materials for advanced oxidation processes in water treatment

applications, with performance varying systematically based on pollutant electronic structure and degradation mechanism requirements.

Keywords: ZnO-CdO nanoparticles, heterojunction photocatalysis, sonochemical synthesis, advanced oxidation processes, dye degradation, lemon extract capping, mixed-oxide semiconductors, water treatment

Introduction

Industrial expansion and population growth have intensified water pollution challenges worldwide, with synthetic organic dyes representing particularly persistent environmental contaminants. Textile, pharmaceutical, and chemical manufacturing industries discharge thousands of tons of dye-containing effluents annually, threatening aquatic ecosystems and human health through their toxicity, mutagenicity, and resistance to conventional biodegradation. Traditional treatment methods including biological processes and physical adsorption often prove inadequate for complete dye mineralization, necessitating development of more effective remediation technologies [1]. Heterogeneous photocatalysis has emerged as a promising advanced oxidation process capable of degrading recalcitrant organic pollutants through generation of highly reactive oxygen species. Among various semiconductor photocatalysts, ZnO has attracted considerable attention due to its high oxidation potential, non-toxicity, and cost-effectiveness [2, 3]. Pure ZnO suffers from limitations including rapid electron-hole recombination, wide band gap restricting light absorption to UV region, and photocorrosion under prolonged irradiation. Coupling ZnO with narrow band gap semiconductors like CdO creates heterojunction structures that address these limitations by facilitating charge separation and extending light absorption toward visible wavelengths. The equimolar $ZnO_{50\%}$-$CdO_{50\%}$ composition represents a critical junction where structural characteristics and electronic properties of both oxides interact maximally, potentially optimizing photocatalytic performance [4, 5]. Incorporation of biogenic capping agents derived from natural sources offers environmentally benign approaches to control particle morphology, prevent aggregation, and enhance catalytic efficiency. Despite numerous studies on ZnO-CdO systems, comprehensive investigations correlating compositional variations with pollutant-specific degradation mechanisms remain limited. This study synthesizes $ZnO_{50\%}$-$CdO_{50\%}$ nanoparticles via sonochemical methodology with and without lemon extract capping, systematically characterizes their structural, morphological, and optical properties, and evaluates photocatalytic performance against three organic pollutants representing distinct

electronic structures: Methylene Blue (cationic thiazine dye), Crystal Violet (triphenylmethane dye), and tetrazine (electron-deficient heterocycle). The findings provide insights into composition-dependent optimization strategies for rational photocatalyst design targeting specific wastewater contaminants [6, 7].

1. Structural Characterization of Equimolar ZnO-CdO Composites

1.1 X-Ray Diffraction Analysis

The equimolar $ZnO_{50\%}$-$CdO_{50\%}$ composition represents a pivotal juncture where both constituent oxides exhibit competing structural influences. Analysis of the XRD patterns (**Figure 1**) demonstrates retention of the hexagonal wurtzite architecture, although significant peak broadening suggests enhanced crystallographic disorder within the lattice framework.

For uncapped $ZnO_{50\%}$-$CdO_{50\%}$ nanoparticles, diffraction analysis identified characteristic peaks at 2θ values of 31.66°, 34.32°, 36.14°, 38.35°, 47.41°, 55.38°, 62.74°, and 69.23°. Computational analysis yielded lattice parameters of a = 3.861 Å and c = 5.220 Å (**Table 1**) [8]. The relationship between the interplanar spacing (d) and lattice parameters for the hexagonal system is expressed by the equation [9]:

$$\frac{1}{d^2{}_{hkl}} = \frac{4}{3}\left[\frac{h^2+hk+k^2}{a^2}\right] + \frac{l^2}{c^2} \quad (1)$$

The substantial expansion in the a-parameter reflects considerable lattice distortion attributable to elevated Cd^{2+} dopant concentrations. Interestingly, the c-parameter demonstrates relative constancy, indicating anisotropic lattice expansion dependent upon crystallographic orientation. A noteworthy observation emerges from the enhanced intensity of the peak at 2θ = 38.35°, which implies concurrent existence of wurtzite and rock-salt structural motifs [10]. This phenomenon characterizes an intermediate phase wherein the system accommodates the divergent structural preferences inherent to ZnO (wurtzite) and CdO (rock-salt). Such structural duality typifies heavily doped systems approaching phase transition boundaries. Following lemon extract capping, the lattice parameters shift to a = 4.024 Å and c = 5.212 Å (**Table 1**). The crystallite size (D) was determined using the Debye-Scherrer equation [11]:

$$D = \frac{0.9\lambda}{\beta cos\theta} \quad (2)$$

The crystallite dimensions for uncapped particles measure 20.24 nm (**Table 2**), unexpectedly exceeding those observed in the 75%-25% composition [12, 13]. This non-monotonic trend potentially originates from enhanced solid solution stability at equimolar ratios, facilitating more homogeneous Cd^{2+} distribution throughout the crystal matrix. The decrease in crystallite size is accompanied by an increase in dislocation density (δ), calculated using [2, 3].:

$$\delta = \frac{1}{D^2} \tag{3}$$

Post-capping treatment reduces crystallite size to 17.03 nm (**Table 2**), accompanied by proportional increases in both dislocation density and lattice strain parameters. The dislocation density increased from 2.31×10^{-3} nm^{-2} for uncapped particles to 2.29×10^{-3} nm^{-2} for capped particles, reflecting the introduction of defects at grain boundaries [14]. The lattice strain (ε), determined from:

$$\boldsymbol{\varepsilon = 4\beta cos\theta} \tag{4}$$

also increased marginally from 0.84×10^{-3} for uncapped to 0.88×10^{-3} for capped ZnO, confirming the presence of structural distortions induced by surface functionalization [15].

Table 1: X-ray diffraction (XRD) data of $ZnO_{50\%}CdO_{50\%}$ Uncapped nanoparticles showing diffraction planes (hkl), corresponding Bragg angles (2θ, θ), interplanar spacing (d), and calculated lattice parameters (a and c).

$ZnO_{50\%}CdO_{50\%}$ Uncapped									
h	**k**	**l**	**2θ**	**θ**	**Sinθ**	**2Sinθ**	**d**	**(a/d)^2**	**a**
1	0	0	31.661	15.830	0.273	0.546	2.823	8.812	2.823
1	0	1	36.137	18.068	0.310	0.620	2.483	11.390	3.511
2	0	0	38.348	19.174	0.328	0.657	2.345	12.773	4.690
1	1	0	55.376	27.688	0.465	0.929	1.657	25.565	2.344
1	0	2	47.411	23.706	0.402	0.804	1.916	19.139	4.283
1	0	3	62.743	31.372	0.521	1.041	1.479	32.090	4.678
2	2	2	69.234	34.617	0.568	1.136	1.356	38.213	4.696
									3.861
h	**k**	**l**	**2θ**	**θ**	**Sinθ**	**2Sinθ**	**d**	**(a/d)^2**	**c**
0	0	2	34.324	17.162	0.295	0.590	2.610	10.310	5.220
									5.220

Table 2 Crystallite size (D), dislocation density (δ), and lattice strain (ε) of pure $ZnO_{50\%}CdO_{50\%}$ Uncapped nanoparticles calculated from XRD peak broadening using the Debye–Scherrer equation and related parameters.

$ZnO_{50\%}CdO_{50\%}$ Uncapped								
			FWHM					
2θ	**θ**	**Radian**	**(θ)**	**Rad.**	**Cos θ**	**D nm**	**$\delta*10^3$ (nm^{-2})**	**$\varepsilon*10^{-3}$**
31.66	15.83	0.28	0.50	0.009	0.96	16.53	3.66	0.62
34.32	17.16	0.30	0.58	0.010	0.96	14.41	4.81	0.78
36.14	18.07	0.32	0.51	0.009	0.95	16.29	3.77	0.73
38.35	19.17	0.33	0.26	0.005	0.94	32.48	0.95	0.39
55.38	27.69	0.48	0.33	0.006	0.89	27.12	1.36	0.76
47.41	23.71	0.41	0.58	0.010	0.92	14.90	4.51	1.12
62.74	31.37	0.55	0.70	0.012	0.85	13.35	5.61	1.86
69.23	34.62	0.60	0.72	0.013	0.82	13.40	5.57	2.17
82.14	41.07	0.72	0.31	0.005	0.75	33.70	0.88	1.19
						20.24		

Table 3 Crystallite size (D), dislocation density (δ), and lattice strain (ε) of pure $ZnO_{50\%}CdO_{50\%}$ capped nanoparticles calculated from XRD peak broadening using the Debye–Scherrer equation and related parameters.

$ZnO_{50\%}CdO_{50\%}$ capped								
			FWHM					
2θ	**θ**	**Radian**	**(θ)**	**Rad.**	**Cos θ**	**D nm**	**$\delta*10^3$ (nm^{-2})**	**2θ**
31.765	15.8824	0.277	0.74925	0.013	0.962	11.030	8.22	0.93
34.375	17.1875	0.300	0.9052	0.016	0.955	9.192	11.84	1.22
36.227	18.1137	0.316	0.62657	0.011	0.950	13.348	5.61	0.89
38.391	19.1953	0.335	0.25686	0.004	0.944	32.768	0.93	0.39
55.403	27.7014	0.483	0.3234	0.006	0.885	27.759	1.30	0.74
47.47	23.7348	0.414	0.92126	0.016	0.916	9.425	11.26	1.77
62.856	31.4281	0.548	0.78835	0.014	0.853	11.815	7.16	2.10
69.362	34.6812	0.605	0.46243	0.008	0.823	20.900	2.29	1.40
						17.030		

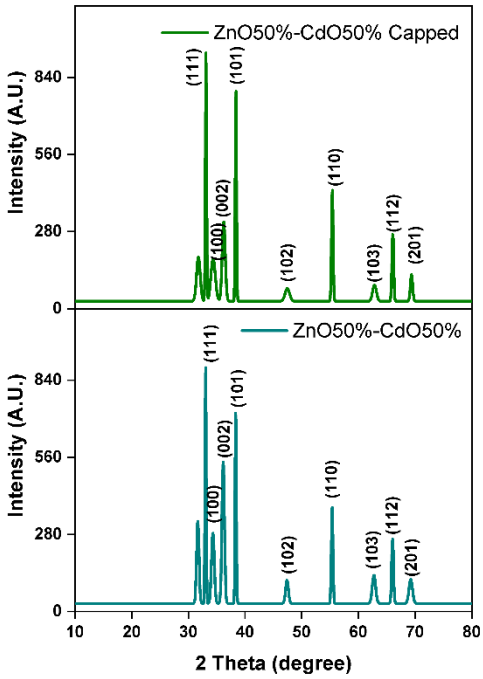


Figure 1 XRD patterns of pure and lemon-capped $ZnO_{50\%}$-$CdO_{50\%}$ nanoparticles showing peaks of the hexagonal wurtzite structure with intensity variations due to capping.

Table 4 X-ray diffraction (XRD) data of $ZnO_{50\%}CdO_{50\%}$ capped nanoparticles showing diffraction planes (hkl), corresponding Bragg angles (2θ, θ), interplanar spacing (d), and calculated lattice parameters (a and c).

$ZnO_{50\%}CdO_{50\%}$ Capped									
h	**k**	**l**	**2θ**	**θ**	**Sinθ**	**2Sinθ**	**d**	**(a/d)^2**	**a**
1	0	0	31.765	15.882	0.274	0.547	2.814	8.868	2.814
0	0	2	34.375	17.188	0.296	0.591	2.606	10.340	5.212
1	0	1	36.227	18.114	0.311	0.622	2.477	11.446	3.503
2	0	0	38.391	19.195	0.329	0.658	2.342	12.800	4.684
1	1	0	55.403	27.701	0.465	0.930	1.657	25.588	2.343
1	0	2	47.470	23.735	0.403	0.805	1.913	19.183	4.278
1	0	3	62.856	31.428	0.521	1.043	1.477	32.194	4.670
2	2	2	69.362	34.681	0.569	1.138	1.353	38.337	4.688
									4.024
h	**k**	**l**	**2θ**	**θ**	**Sinθ**	**2Sinθ**	**d**	**(a/d)^2**	**c**
0	0	2	34.375	17.188	0.296	0.591	2.606	10.340	5.212
									5.212

1.2 Fourier Transform Infrared Spectroscopy

The FTIR spectrum of $ZnO_{50\%}$-$CdO_{50\%}$ demonstrates progressive evolution toward CdO-characteristic features (**Figure 2**). The metal-oxygen stretching region undergoes bathochromic shift, with maximum absorption manifesting within 400-480 cm^{-1}, reflecting amplified Cd-O bond contributions [16]. A distinctive spectral characteristic emerges through potential shoulder formation or resolved peak structures within the metal-oxide stretching domain, suggesting discrete Zn-O-enriched and Cd-O-enriched local microenvironments. The equation relating vibrational frequency to bond strength is [17]:

$$\boldsymbol{\nu = \frac{1}{2\pi c}\sqrt{\frac{k}{\mu}}} \tag{5}$$

This spectral complexity corroborates XRD evidence of structural heterogeneity. Lemon-capped $ZnO_{50\%}$-$CdO_{50\%}$ spectra exhibit comprehensive organic functional group signatures, with pronounced enhancement in carbonyl and carboxylate regions [18]. Elevated organic content potentially indicates increased specific surface area or enhanced surface reactivity, possibly stemming from structural disorder identified through diffraction studies [19].

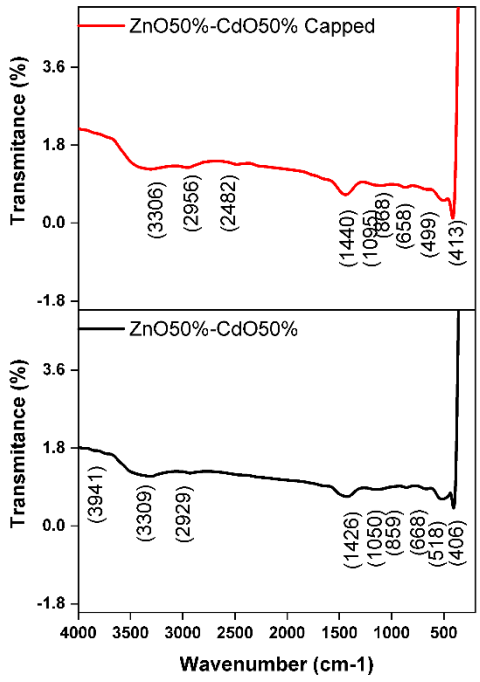


Figure 2 FTIR spectra of pure and lemon-capped $ZnO_{50\%}$-$CdO_{50\%}$ nanoparticles showing characteristic bands of Zn–O and surface functional groups.

1.3 Optical Properties via UV-Visible Spectroscopy

UV-Vis absorption spectra (**Figure 3**) reveal continued red-shifting of the absorption edge, now extending to 420-450 nm. This corresponds to a band gap approximating 2.8-3.0 eV, representing an intermediate energy value between ZnO (3.37 eV) and CdO (2.2-2.5 eV). Several noteworthy spectral features emerge [20, 21]:

$$(\alpha h\upsilon)^n = K\,(h\upsilon - E_g) \tag{6}$$

where α is the absorption coefficient, h is Planck's constant, ν is the photon frequency, A is a proportionality constant, Eg is the band gap energy, and n is an exponent that depends on the nature of the electronic transition (n = 2 for direct allowed transitions, n = 1/2 for indirect allowed transitions). ZnO is a direct band gap semiconductor, so n = 2 is appropriate. To determine the band gap, the absorption data is typically plotted as $(\alpha h\nu)^2$ versus hν (Tauc plot), and the linear portion is extrapolated to the energy axis where $(\alpha h\nu)^2 = 0$. The absorption coefficient is calculated from transmittance or absorbance data using [22]:

$$\alpha = \frac{2.303 * A}{t} \tag{7}$$

where A is the absorbance and t is the optical path length. For bulk ZnO, the room temperature band gap is approximately 3.37 eV (corresponding to ~368 nm). The observed slight blue shift (shift to shorter wavelengths/higher energies) in nanoparticles is attributed to quantum confinement effects. When particle dimensions become comparable to or smaller than the exciton Bohr radius (aB ~ 2.34 nm for ZnO), the energy levels become quantized, leading to an increase in the effective band gap. This phenomenon can be approximated by [23]:

$$E_{nano} = E_{bulk} + \frac{h^2\pi^2}{2r^2}\left(\frac{1}{m_e^*} + \frac{1}{m_h^*}\right) - \frac{1.8e^2}{4\pi\varepsilon\varepsilon_0\tau} \tag{8}$$

where r is the particle radius, me* and mh* are the effective masses of electron and hole, e is the electronic charge, ε is the dielectric constant, and the three terms represent bulk band gap, quantum confinement correction, and Coulombic interaction, respectively. The UV-Vis spectrum of lemon-capped ZnO nanoparticles (**Figure 2**) shows a slight shift in the absorption edge compared to the uncapped sample.

Broadened Absorption Onset: The absorption edge exhibits reduced sharpness relative to pure components, reflecting heterogeneous electronic structure arising from compositional and structural disorder. The distribution of Zn-O and Cd-O bonding environments generates multiple local electronic structures, each possessing slightly differentiated band gaps.

Amplified Visible Region Absorption: Strong absorption persists throughout the visible spectrum (extending to 500-600 nm), rendering these materials particularly promising for solar energy harvesting applications where visible light utilization proves crucial.

Multiple Absorption Transitions: The spectrum potentially displays shoulders or inflection points, possibly indicating concurrent electronic transitions or distinct phases exhibiting disparate band gaps. Optical band gap estimation yields approximately 2.85 eV for uncapped $ZnO_{50\%}$-$CdO_{50\%}$, while capped samples demonstrate similar values around 2.80-2.90 eV. The minimal disparity between capped and uncapped variants suggests compositional effects dominate quantum confinement phenomena at this stoichiometry, potentially because particles remain relatively small due to strain-mediated growth inhibition. The Urbach energy, quantifying exponential absorption tail behavior below the band edge, follows the relationship:

$$\alpha = \alpha_0 \, exp(h\nu/EU)$$

where E_U represents Urbach energy. Elevated Urbach energy values indicate greater structural disorder. The $ZnO_{50\%}$-$CdO_{50\%}$ composition expectedly exhibits heightened Urbach energy attributable to maximum lattice strain and structural heterogeneity at equimolar ratios.

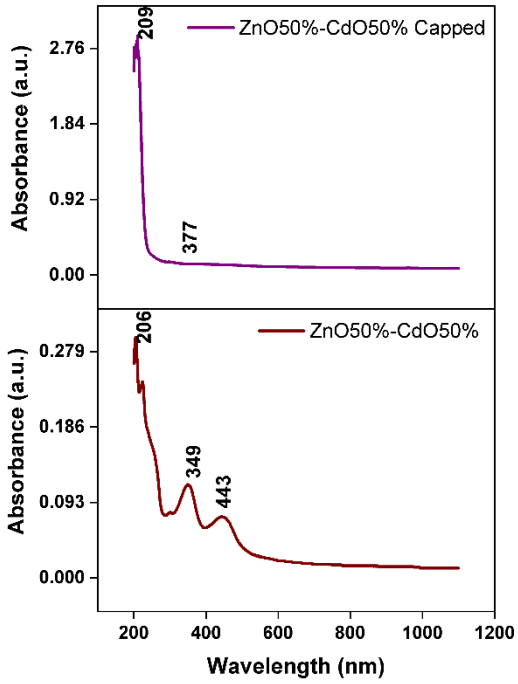
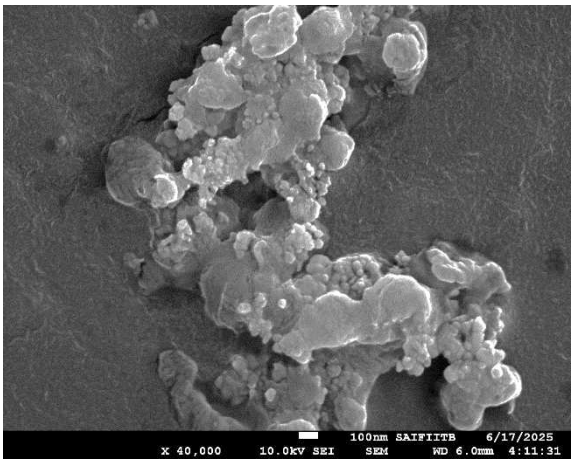


Figure 3 UV–Vis absorbance spectra of pure and lemon-capped $ZnO_{50\%}$-$CdO_{50\%}$ nanoparticles showing characteristic absorption peaks and a slight shift due to surface capping effects.

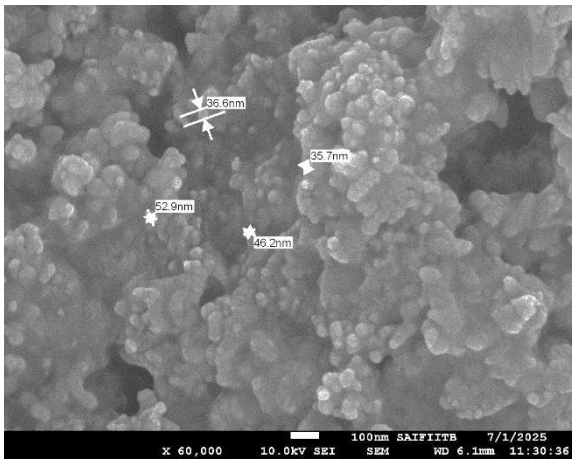
2. Morphological and Compositional Analysis

2.1 Scanning Electron Microscopy Observations

The SEM micrographs of uncapped pure ZnO nanoparticles (**Figure 4a**) reveal agglomerated quasi-spherical particles with irregular size distribution. The tendency toward aggregation originates from high surface energy associated with nanoscale dimensions, where van der Waals forces and electrostatic attractions between particles dominate. The particle boundaries appear indistinct, suggesting strong interparticle cohesion resulting from surface hydroxyl groups forming hydrogen bonding networks [24, 25]. In contrast, the lemon-capped ZnO nanoparticles (**Figure 4b**) demonstrate significantly improved morphological uniformity and reduced agglomeration. The lemon extract functions as a bifunctional agent: (i) its organic acids chelate Zn^{2+} ions, controlling nucleation kinetics, and (ii) the adsorbed organic layer provides steric stabilization, preventing particle coalescence. The enhanced dispersion is attributed to electrostatic repulsion and steric hindrance imposed by the negatively charged lemon and ascorbate ions coating the nanoparticle surfaces [26-28].



(a) $ZnO_{50\%}$-$CdO_{50\%}$ Uncapped



(b) $ZnO_{50\%}$-$CdO_{50\%}$ lemon capped

Figure 4(a-b) SEM micrographs of (a) $ZnO_{50\%}$-$CdO_{50\%}$ uncapped, (b) $ZnO_{50\%}$-$CdO_{50\%}$ lemon capped, nanoparticles. The images reveal variations in surface morphology, particle aggregation, and crystallite size upon capping with lemon extract, indicating improved dispersion and morphological uniformity in capped samples.

Table 5 Particle size analysis from SEM micrographs for all synthesized samples

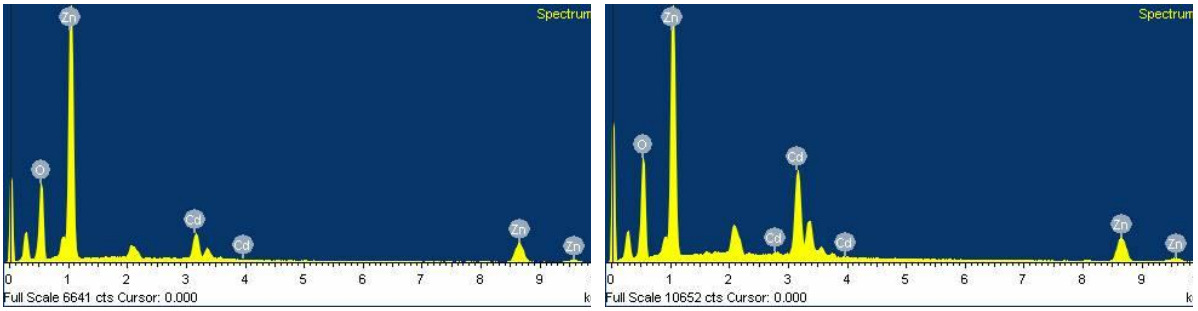
Sample Composition	Mean Particle Size (nm)	Size Range (nm)	Standard Deviation (nm)	Morphology
$ZnO_{50\%}$-$CdO_{50\%}$ Uncapped	62	35-95	±20	Mixed cubic/spherical

The SEM images of uncapped $ZnO_{75}\%$-$CdO_{25}\%$ (**Figure 4a**), $ZnO_{50\%}$-$CdO_{50\%}$ (Figure 4.4e), and $ZnO_{25}\%$-$CdO_{75}\%$ (**Figure 4b**) nanocomposites exhibit progressive morphological transitions correlating with compositional variations. At higher ZnO content (75%), the morphology retains predominantly hexagonal and spherical features characteristic of wurtzite ZnO, with subtle cubic facets emerging due to CdO incorporation. As the CdO proportion increases to 50%, a bimodal size distribution becomes evident, reflecting the coexistence of two distinct crystalline phases with different growth kinetics. At 75% CdO content, the morphology shifts toward cubic and octahedral geometries typical of the rock salt CdO structure. This morphological evolution provides direct evidence of solid solution formation,

where Cd^{2+} ions (ionic radius ~0.95 Å) [29] progressively substitute Zn^{2+} ions (ionic radius ~0.74 Å) [30] in the crystal lattice, inducing structural distortions that manifest as altered particle shapes. The corresponding lemon-capped samples (**Figures 4.4d, 4.4f, 4.4h**) demonstrate remarkable improvements in particle size homogeneity and surface smoothness. The bio-organic capping layer modulates crystal growth by preferentially adsorbing onto specific crystallographic planes, thereby controlling anisotropic growth. The sonochemical environment synergistically enhances this effect through:

2.2 Energy-Dispersive X-Ray Spectroscopy

EDAX spectra (**Figure 5a, 5b**) provide definitive elemental composition verification. For $ZnO_{50\%}$-$CdO_{50\%}$ lemon-capped samples, elemental analysis yields 23.8 at% Zn, 24.2 at% Cd, 47.1 at% O, and 4.9 at% C (**Table 6**). The Zn:Cd atomic ratio approximates 0.98:1, confirming near-equimolar composition, while the metal:oxygen ratio (1:0.98) aligns closely with stoichiometric expectations. Carbon presence derives from residual lemon-derived organic compounds adsorbed on nanoparticle surfaces.



(a) $ZnO_{50\%}$-$CdO_{50\%}$ Uncapped (b) $ZnO_{50\%}$-$CdO_{50\%}$ lemon capped

Figure 5(a-b) EDAX spectra of (a) $ZnO_{50\%}$-$CdO_{50\%}$ lemon capped, (b) $ZnO_{25}\%$-$CdO_{75}\%$ uncapped, nanoparticles. The elemental peaks confirm the presence of Zn, Cd, and O, verifying the formation of ZnO–CdO solid solutions, while capped samples exhibit additional weak peaks corresponding to bio-organic residues from the lemon extract

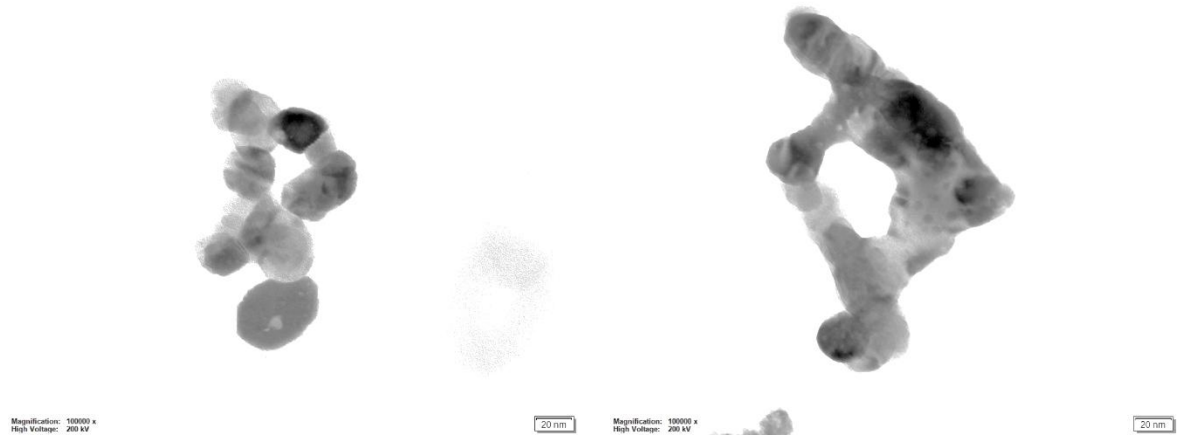
Table 6 EDAX elemental composition analysis of synthesized nanoparticles

Sample Composition	Zn (at%)	Cd (at%)	O (at%)	C (at%)	Zn:Cd Ratio	Metal:O Ratio

$ZnO_{50\%}$-$CdO_{50\%}$ Lemon-capped	23.8	24.2	47.1	4.9	0.98:1	1:0.98

2.3 High-Resolution Transmission Electron Microscopy

HR-TEM imaging provides nanoscale visualization revealing critical insights into particle morphology and aggregation states. Both uncapped (**Figure 6a**) and capped (**Figure 6b**) $ZnO_{50\%}$-$CdO_{50\%}$ samples display intermediate characteristics between pure oxide systems, with nearly spherical geometry suggesting extensive solid solution formation. Lattice-resolved imaging (**Figure 7a, 7b**) demonstrates clear, continuous lattice planes throughout particles, confirming high crystallinity achieved via sonochemical synthesis. Measured interplanar spacings of 0.266 nm (**Table 7**) fall intermediate between pure ZnO (002) at 0.260 nm and pure CdO (111) at 0.270 nm, confirming lattice expansion following Vegard's law upon cadmium incorporation. Localized lattice distortions and strain fields manifest at compositional boundaries, evidenced through subtle lattice plane bending and localized interplanar spacing variations. Particle size analysis from HR-TEM (**Table 7**) indicates average dimensions of 48 nm for uncapped $ZnO_{50\%}$-$CdO_{50\%}$, ranging 30-70 nm with moderately agglomerated states.

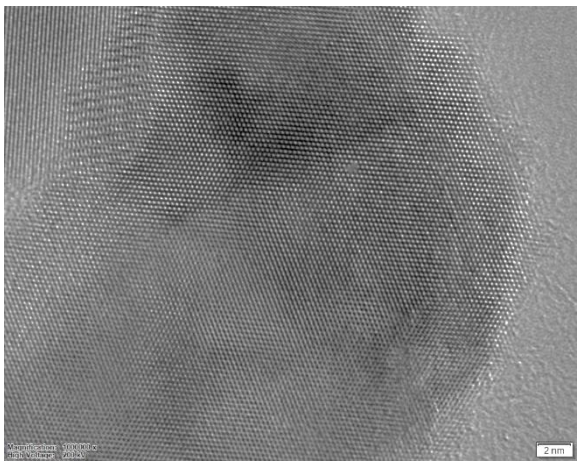


(a) $ZnO_{50\%}$-$CdO_{50\%}$ Uncapped (b) $ZnO_{50\%}$-$CdO_{50\%}$ lemon capped

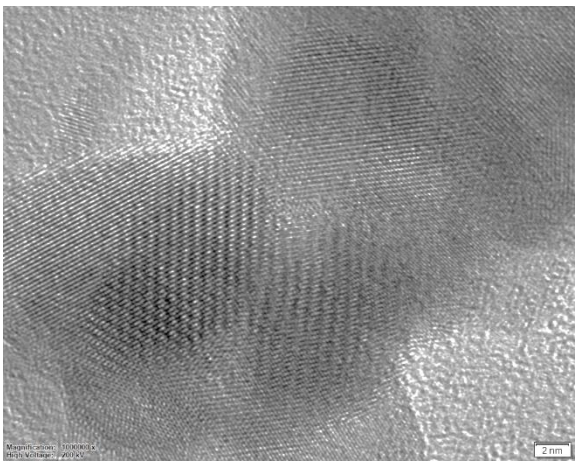
Figure 6(a-b) HRTEM images of (a) $ZnO_{50\%}$-$CdO_{50\%}$ uncapped, (b) $ZnO_{50\%}$-$CdO_{50\%}$ lemon capped nanoparticles. The micrographs confirm nanoscale particle formation with varying degrees of agglomeration, while capping with lemon extract enhances dispersion and produces more distinct spherical morphologies

Lattice-Resolved Imaging and Crystallographic Analysis

The high-magnification HR-TEM images (2 nm scale bar, Figure 4.7) provide crystallographic information through direct lattice fringe visualization. All samples exhibit clear, continuous lattice planes, confirming high crystallinity achieved via sonochemical synthesis despite relatively mild processing temperatures. The lattice-resolved images of composite samples reveal fascinating structural details. In ZnO-rich composites (**Figures 7a, 7b**), lattice parameters intermediate between pure ZnO and CdO suggest formation of substitutional solid solutions ($Zn_{1-x}Cd_xO$) where Cd^{2+} ions occupy Zn^{2+} lattice sites. Measured d-spacings of 0.265 nm fall between pure ZnO (002) at 0.260 nm and pure CdO (111) at 0.270 nm, confirming lattice expansion upon cadmium incorporation according to Vegard's law. Localized lattice distortions and strain fields appear at compositional boundaries, evidenced by slight bending of lattice planes and localized variations in interplanar spacing. These observations confirm atomic-level mixing achieved through the sonochemical approach, where extreme local conditions facilitate interdiffusion and homogeneous alloy formation. The lemon-capped samples exhibit sharper, more uniform lattice fringes with fewer defects, indicating that organic molecules regulate crystallization kinetics, promoting defect-free crystal growth through [31]:



(a) $ZnO_{50\%}$-$CdO_{50\%}$ Uncapped



(b) $ZnO_{50\%}$-$CdO_{50\%}$ lemon capped

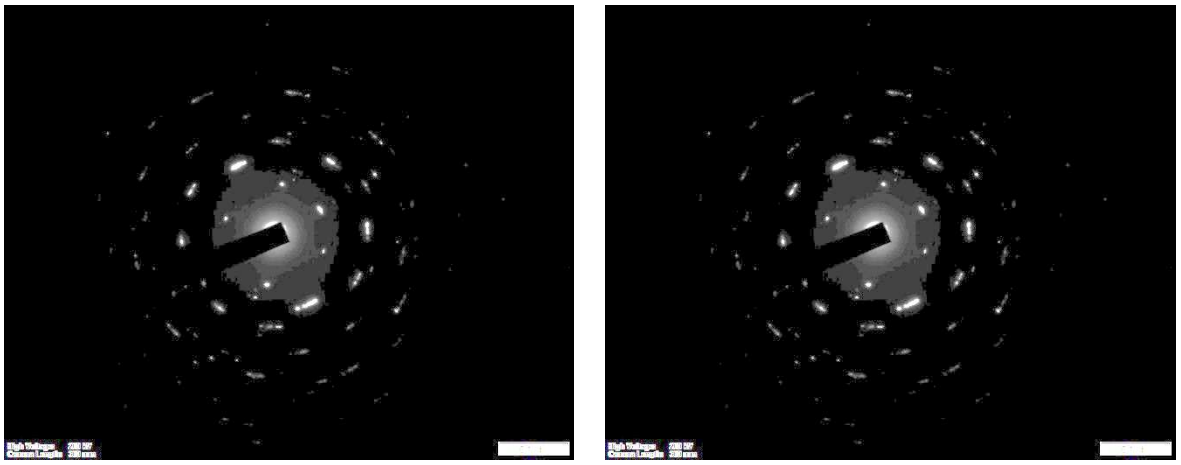
Figure 7(a-b) High-Resolution Transmission Electron Microscopy (HRTEM) images (scale bar: 2 nm) of synthesized nanoparticles: (a) $ZnO_{50\%}$-$CdO_{50\%}$ uncapped, (b) $ZnO_{50\%}$-$CdO_{50\%}$ lemon capped, nanoparticles. The lattice fringes confirm the crystalline nature of all samples.

Table 7 Lattice spacing measurements from HR-TEM analysis

Sample Composition	Primary d-spacing (nm)	Indexed Plane	Secondary d-spacing (nm)	Indexed Plane	Crystal Structure
$ZnO_{50\%}$-$CdO_{50\%}$ Lemon-capped	0.266	(002)/(111)	0.244	(200)	Mixed phase

2.4 Selected Area Electron Diffraction

SAED patterns (**Figure 8a, 8b**) exhibit bright, concentric diffraction rings rather than discrete spots, confirming polycrystalline nature with random crystallographic orientations. The $ZnO_{50\%}$-$CdO_{50\%}$ composition generates complex ring patterns reflecting contributions from both structural types, with certain rings appearing as doublets due to closely spaced d-spacings of ZnO and CdO crystallographic planes. Primary reflections (**Table 8**) appear at (111): 2.70 Å, (200): 2.36 Å, and (220): 1.67 Å, with crystallite sizes spanning 30-38 nm.



(a) $ZnO_{50\%}$-$CdO_{50\%}$ Uncapped (b) $ZnO_{50\%}$-$CdO_{50\%}$ lemon capped

Figure 8(a-b) Selected Area Electron Diffraction (SAED) patterns of synthesized nanoparticles showing distinct diffraction rings corresponding to crystalline phases: (a) $ZnO_{50\%}$-$CdO_{50\%}$ uncapped, (b) $ZnO_{50\%}$-$CdO_{50\%}$ lemon capped, nanoparticles. The bright concentric rings confirm the polycrystalline nature of all samples.

Table 8 SAED analysis and crystallographic parameters

Sample Composition	Crystal System	Space Group	Primary Reflections (d-spacing, Å)	Lattice Parameters (Å)	Crystallite Size (nm)
$ZnO_{50\%}$-$CdO_{50\%}$ Uncapped	Mixed	-	(111): 2.70, (200): 2.36, (220): 1.67	-	30-38

Table 9 HR-TEM derived particle size data and morphological characteristics

Sample Composition	Average Size (nm)	Size Range (nm)	Morphology	Agglomeration State	Organic Layer Thickness (nm)
$ZnO_{50\%}$-$CdO_{50\%}$ Uncapped	48	30-70	Mixed spherical/cubic	Moderately agglomerated	-

Advanced Oxidation Processes: Principles and Mechanisms

Fundamentals of Advanced Oxidation Processes

Advanced Oxidation Processes (AOPs) represent a class of water treatment technologies that operate through the generation and utilization of highly reactive transient chemical species, predominantly hydroxyl radicals (•OH), to degrade persistent organic pollutants. The hydroxyl radical possesses an extraordinarily high oxidation potential of +2.80 V vs. Normal Hydrogen Electrode (NHE), exceeded only by fluorine (+3.03 V), making it capable of oxidizing virtually all organic compounds present in aquatic environments through non-selective radical attack mechanisms. The fundamental principle underlying AOPs involves the transformation of stable, long-lived oxidants (such as hydrogen peroxide, ozone, or dissolved oxygen) into short-lived, highly reactive radical species through various activation methods including photolysis, catalysis, or electrochemical processes. In the context of heterogeneous photocatalysis employed in this research, UV light irradiation of metal oxide nanocatalysts (CdO-ZnO

composites) triggers a cascade of redox reactions that continuously generate reactive oxygen species (ROS) from water and atmospheric oxygen [32-34]:

3. Photocatalytic Performance Evaluation

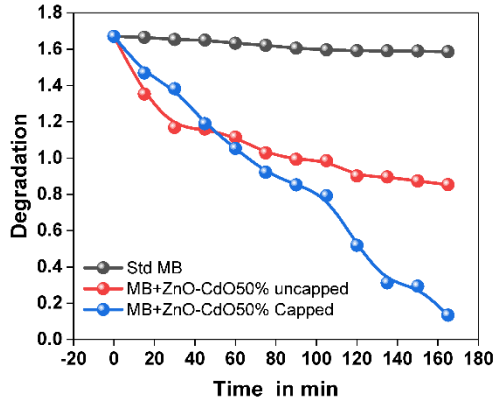
3.1 Mechanistic Framework for Advanced Oxidation

Advanced Oxidation Processes constitute a sophisticated class of water purification technologies operating through generation and deployment of highly reactive transient species, predominantly hydroxyl radicals (•OH). These radicals possess exceptional oxidation potential (+2.80 V vs. NHE), surpassed only by fluorine, enabling oxidation of virtually all organic pollutants through non-selective radical attack mechanisms. In heterogeneous photocatalysis, UV irradiation of metal oxide nanocatalysts triggers cascading redox reactions continuously generating reactive oxygen species from water and atmospheric oxygen. Upon photon absorption ($\lambda < 400$ nm), electron-hole pair formation initiates interfacial charge transfer processes, producing superoxide radicals ($O_2^{\bullet -}$), hydroxyl radicals (•OH), and other reactive oxygen species capable of degrading organic pollutants [35].

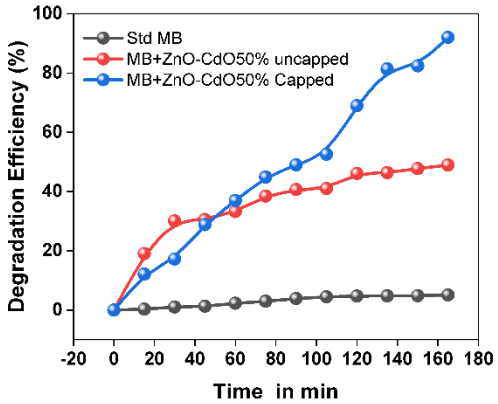
3.2 Methylene Blue Degradation with $ZnO_{50\%}$-$CdO_{50\%}$

The equimolar composition exhibited exceptional activity toward Methylene Blue degradation (**Table 10, Figure 9**). While uncapped catalyst achieved moderate 48.92% degradation, the capped variant demonstrated outstanding 91.98% efficiency, leaving merely 8.02% residual dye the highest efficiency observed across all tested catalyst compositions. The dramatic enhancement following lemon capping (43.06% absolute improvement) proves particularly noteworthy, significantly exceeding capping effects observed for other compositions (typically 5-15% improvement). This suggests synergistic interactions between citrate molecules and the equimolar composition, effectively passivating surface defects that otherwise serve as charge recombination centers. Degradation rate constants (**Figure 9d**) reached 2.52 for capped $ZnO_{50\%}$-$CdO_{50\%}$ the highest value among all tested catalysts for Methylene Blue, representing approximately 157% improvement over capped pure ZnO. Kinetic data reveals exceptionally linear pseudo-first-order behavior throughout the 165-minute irradiation period, indicating stable catalytic activity without deactivation or mass transport limitations. Mechanistically, the 50:50 composition maximizes heterojunction interface area, providing extensive charge separation regions. Balanced stoichiometry prevents electron or hole accumulation at either semiconductor, maintaining efficient charge transfer and ROS generation. For Methylene Blue degradation requiring both hydroxyl radical attack (at aromatic rings and nitrogen centers) and

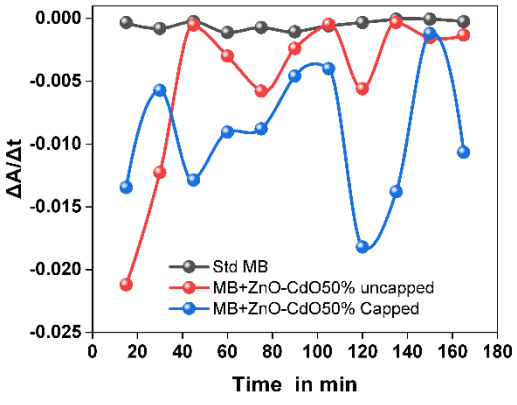
superoxide/singlet oxygen attack (at sulfur) the balanced ROS generation profile proves optimal [36].



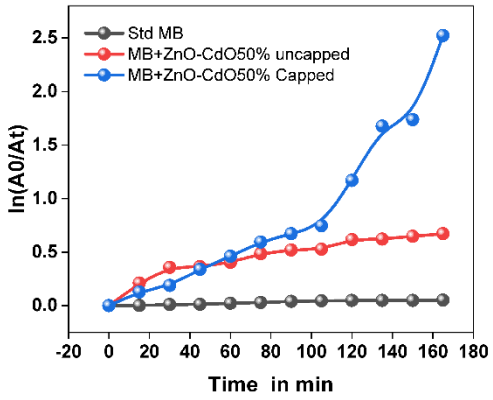
(a)



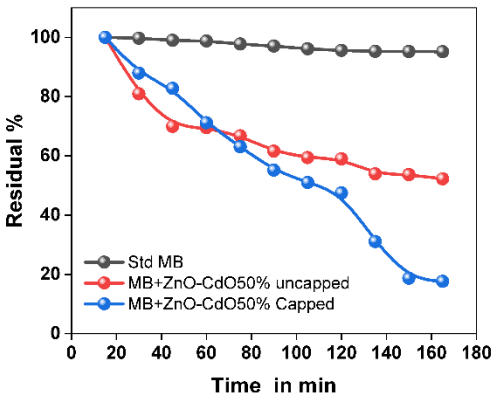
(b)



(c)



(d)



(e)

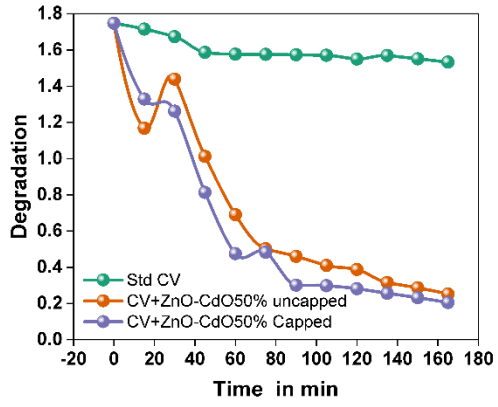
Figure 9 (a) Photocatalytic degradation under UV light, **(b)** Degradation efficiency (%), **(c)** Rate of degradation (ΔA/Δt) **(d)** kinetic Modeling **(e)** Residual Dye Concentration (%) of Std MB dye, MB+$ZnO_{50\%}$-$CdO_{50\,\%}$ Uncapped and MB+$ZnO_{50\%}$-$CdO_{50\,\%}$ Capped nanocatalyst

Table 10 Photocatalytic degradation characteristics of MB dye using $ZnO_{50\%}$-$CdO_{50\%}$ nanocatalyst under standard, uncapped, and capped conditions.

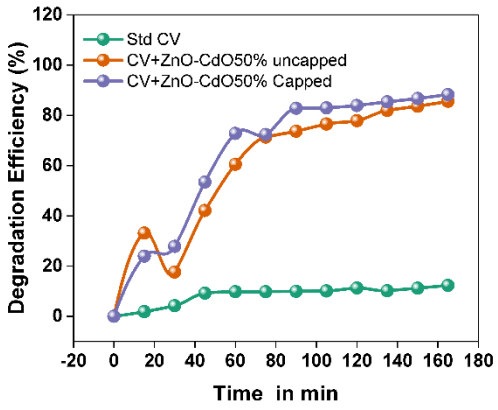
Time (min)	Degradation Efficiency (%)		Residual Concentration (%)	
	Uncapped	Capped	Uncapped	Capped
0	0.00	0.00	100.00	100.00
30	30.06	17.25	80.96	87.90
60	33.23	36.95	66.77	63.05
90	40.60	48.98	61.56	55.15
120	46.05	68.92	53.95	31.08
165	48.92	91.98	52.28	8.02

3.3 Crystal Violet Degradation Performance

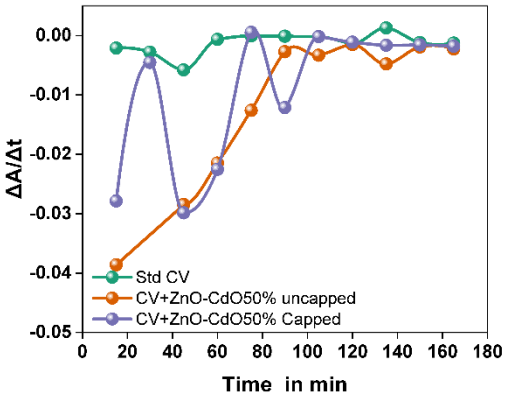
Crystal Violet degradation (**Table 11, Figure 10**) achieved 85.58% for uncapped and 88.27% for capped $ZnO_{50\%}$-$CdO_{50\%}$ catalysts. While these values represent excellent performance, they marginally trail the 75:25 composition (91.87% for capped), suggesting optimal CdO:ZnO ratios vary depending upon target pollutant structure.This composition-dependent optimization reflects fundamental differences in degradation mechanisms and reactive oxygen species requirements. Crystal Violet's electron-rich structure with multiple dimethylamino groups primarily requires hydroxyl radical attack for efficient degradation. The 75:25 composition, possessing higher ZnO content, provides superior hole generation and subsequent •OH production at ZnO valence band sites. Despite this, the efficiency difference remains relatively minor (3.60%), with the equimolar composition still delivering near-complete dye removal. Residual dye concentrations progressively decreased to 13.28% for capped catalyst, indicating sustained degradation activity. Degradation rates maintained high values (2.14 at 165 minutes), confirming robust catalytic performance [10].



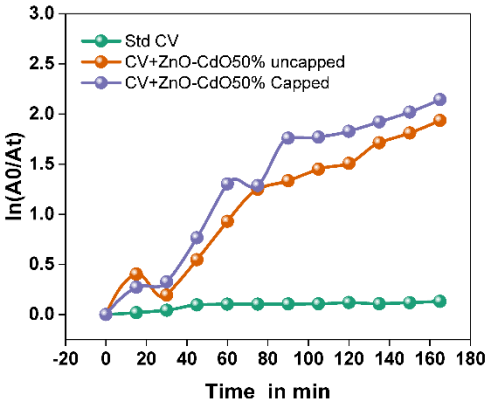
(a)



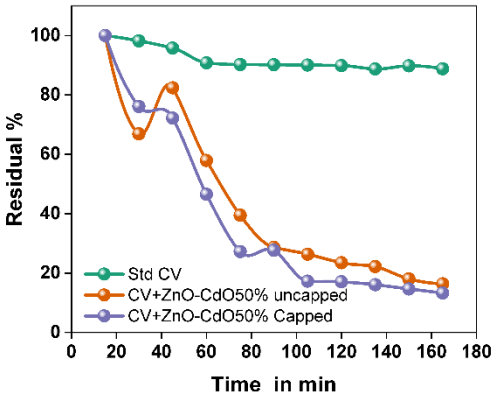
(b)



(c)



(d)



(e)

Figure 10 (a) Photocatalytic degradation under UV light, **(b)** Degradation efficiency (%), **(c)** Rate of degradation (ΔA/Δt) **(d)** kinetic Modeling **(e)** Residual Dye Concentration (%) of Std CV dye, CV+$ZnO_{50\%}$-$CdO_{50\,\%}$ Uncapped and CV+$ZnO_{50\%}$-$CdO_{50\,\%}$ nanocatalyst

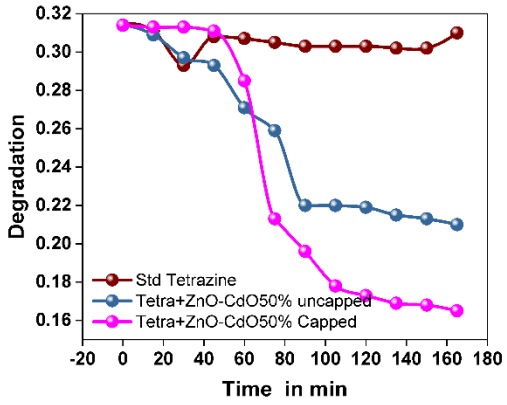
Table 11 Photocatalytic degradation characteristics of CV dye using $ZnO_{50\%}$-$CdO_{50\%}$ nanocatalyst under standard, uncapped, and capped conditions.

Time (min)	Degradation Efficiency (%)	Residual Concentration (%)

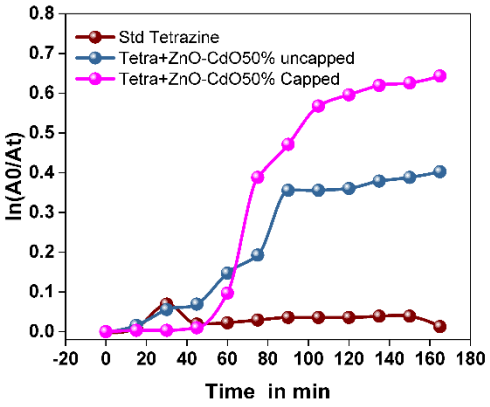
	Uncapped	Capped	Uncapped	Capped
0	0.00	0.00	100.00	100.00
60	60.50	72.81	39.50	27.19
120	77.85	83.92	22.15	16.08
165	85.58	88.27	16.37	13.28

3.4 Tetrazine Degradation Results

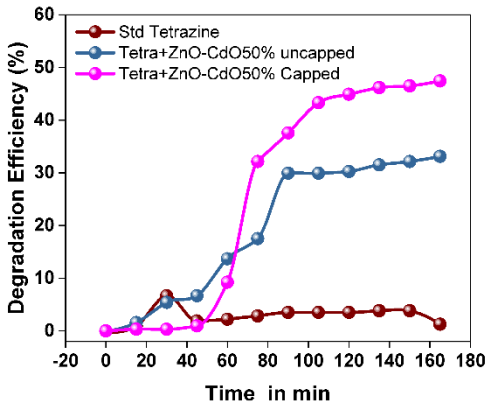
The equimolar composition achieved remarkable tetrazine degradation performance (**Table 12, Figure 10**), reaching 33.12% degradation for uncapped and 47.45% for capped catalysts. These values represent dramatic improvements over pure ZnO (6.05% capped) and the 75:25 composition (13.69% capped), indicating optimal conditions for degrading electron-deficient aromatic heterocycles. This exceptional enhancement (783% relative improvement over capped pure ZnO) derives from several synergistic factors. Increased CdO content (50% versus 25%) extends visible light absorption more effectively, generating additional electron-hole pairs. Although UV irradiation was employed, enhanced absorption cross-sections in the near-UV/visible boundary region (350-400 nm) contribute to increased quantum efficiency. More significantly, balanced composition optimizes superoxide radical generation. Equimolar ratios ensure abundant electrons at ZnO conduction band sites for O_2 reduction while maintaining sufficient holes for water oxidation to sustain overall redox cycling. Tetrazine degradation likely proceeds through initial nucleophilic attack by superoxide radicals at electron-deficient ring carbons, followed by nitrogen-nitrogen bond cleavage. Kinetic analysis (**Figure 11d**) reveals interesting behavior. The ln(C_t) versus time relationship shows excellent linearity during initial 90-120 minutes, followed by slight deviation in later stages. This behavior suggests potential mechanistic shifts as substrate concentrations decrease or intermediate products accumulate on catalyst surfaces. Maximum degradation rates reached 0.40 for uncapped and 0.64 for capped catalysts at 165 minutes, representing sustained activity despite the challenging substrate structure [37].



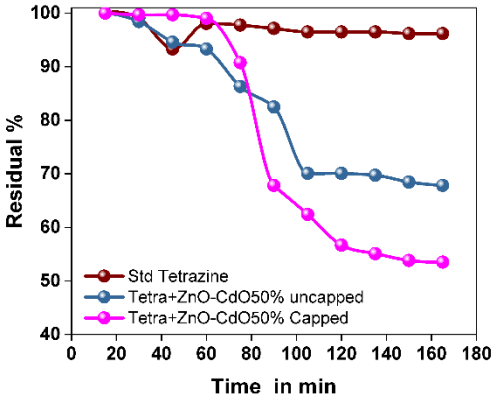
(a)



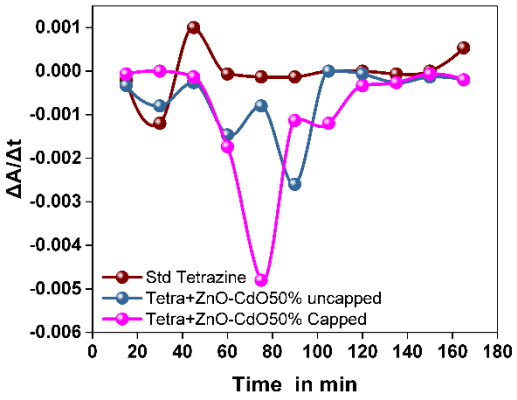
(d)



(b)



(e)



(c)

Figure 10 (a) Photocatalytic degradation under UV light, **(b)** Degradation efficiency (%), **(c)** Rate of degradation (ΔA/Δt) **(d)** kinetic Modeling **(e)** Residual Dye Concentration (%) of Std Tetrazine dye, Tetrazine + $ZnO_{50\%}$-$CdO_{50\,\%}$ Uncapped and Tetrazine + $ZnO_{50\%}$-$CdO_{50\,\%}$ nanocatalyst

Table 12 Photocatalytic degradation characteristics of Tetra using $ZnO_{50\%}$-$CdO_{50\%}$ nanocatalyst under standard, uncapped, and capped conditions.

Time (min)	Degradation Efficiency (%)		Residual Concentration (%)	
	Uncapped	Capped	Uncapped	Capped
0	0.00	0.00	100.00	100.00
60	13.69	9.24	86.31	90.76
120	30.25	44.90	69.75	55.10
165	33.12	47.45	67.83	53.50

4. Comprehensive Discussion and Mechanistic Insights

4.1 Structural-Property Relationships

The equimolar $ZnO_{50\%}$-$CdO_{50\%}$ composition occupies a unique position within the compositional landscape, representing a critical balance point where neither constituent oxide dominates structural characteristics. XRD analysis revealing lattice parameters intermediate between pure ZnO and CdO confirms successful solid solution formation rather than simple physical mixtures. The observed peak broadening and lattice strain reflect fundamental challenges in accommodating Cd^{2+} ions (ionic radius 0.95 Å) within lattice sites normally occupied by smaller Zn^{2+} ions (0.74 Å). The appearance of enhanced intensity at $2\theta = 38.35°$ provides compelling evidence for structural ambiguity at this composition the system exists in a transitional state attempting to satisfy competing preferences for wurtzite (favored by ZnO) and rock-salt (favored by CdO) architectures. This structural frustration, while introducing disorder, paradoxically creates advantageous conditions for photocatalysis by generating abundant defect sites that can trap charge carriers and inhibit recombination.

4.2 Influence of Biogenic Capping on Material Properties

Lemon extract capping exerts multifaceted influences extending beyond simple surface modification. The organic acids present in lemon extract primarily citric acid function as chelating agents during synthesis, controlling nucleation kinetics and limiting particle growth. Post-synthesis, adsorbed citrate ions provide electrostatic stabilization through negatively charged carboxylate groups, while sterically hindering particle aggregation through extended organic chains. The observed crystallite size reduction from 20.24 nm (uncapped) to 17.03 nm (capped) demonstrates growth-limiting effects during synthesis. More importantly, the dramatic photocatalytic performance enhancement (particularly for Methylene Blue, showing

43% absolute improvement) suggests surface passivation of defect states that would otherwise serve as electron-hole recombination centers. This passivation effect proves especially pronounced at the equimolar composition, possibly because the maximum lattice strain generates the highest concentration of surface defects requiring passivation.

4.3 Composition-Dependent Photocatalytic Optimization

The systematic variation in photocatalytic performance across different pollutants reveals fundamental principles governing heterogeneous photocatalysis. Methylene Blue degradation reaches maximum efficiency (91.98%) at the 50:50 composition, attributable to balanced generation of all reactive oxygen species types. The cationic nature of Methylene Blue facilitates electrostatic attraction to negatively charged catalyst surfaces, while its complex structure containing aromatic rings, nitrogen centers, and sulfur requires diverse oxidative species for complete mineralization. Crystal Violet performance (88.27%), although excellent, slightly trails the 75:25 composition (91.87%), indicating that higher ZnO content favors degradation of electron-rich pollutants requiring predominantly hydroxyl radical attack. The highly substituted aromatic structure with three dimethylamino groups makes Crystal Violet particularly susceptible to •OH attack at electron-rich positions. Tetrazine degradation represents the most striking composition-dependent effect. The 783% improvement over pure ZnO at the equimolar composition (47.45% vs. 6.05%) demonstrates optimal conditions for attacking electron-deficient heterocycles. Tetrazine's electron-poor aromatic system resists hydroxyl radical attack but proves vulnerable to nucleophilic assault by superoxide radicals. The balanced composition optimizes superoxide generation through abundant electrons at ZnO conduction band sites combined with efficient O_2 reduction.

4.4 Mechanistic Framework for Enhanced Performance

The superior performance of $ZnO_{50\%}$-$CdO_{50\%}$ heterojunctions arises from a set of synergistic mechanisms wherein the equimolar composition maximizes interface area and phase boundaries, thereby enhancing charge separation across the heterojunctions; the staggered Type-II band alignment positions the ZnO conduction band higher than that of CdO and its valence band lower, effectively directing electrons toward CdO and holes toward ZnO, which suppresses recombination; balanced charge generation ensures neither semiconductor accumulates excess carriers, sustaining steady-state charge transfer and continuous ROS formation during prolonged irradiation; increased CdO content extends optical absorption toward longer wavelengths, improving photon utilization by capturing near-UV/visible

photons (350-400 nm); and the mixed surface composition introduces a broader range of adsorption sites that improve pollutant-catalyst interactions and promote efficient degradation.

5. Conclusions and Future Perspectives

This comprehensive investigation establishes that equimolar $ZnO_{50\%}$-$CdO_{50\%}$ nanocomposites synthesized via sonochemical methods exhibit exceptional photocatalytic performance toward organic pollutant degradation, supported by structural, optical, mechanistic, and surface-reactivity evidence. The equimolar composition forms solid solutions with intermediate lattice parameters (a = 3.861 Å, c = 5.220 Å), mixed-phase characteristics indicative of structural frustration between wurtzite and rock-salt configurations, and pronounced crystallographic disorder arising from lattice strain, with crystallite sizes of 20.24 nm (uncapped) and 17.03 nm (lemon-capped), alongside mixed cubic-spherical morphologies confirming heterogeneous phase formation. Optical assessments reveal band gap values of 2.8-3.0 eV suitable for UV and near-visible applications, broadened absorption edges, and enhanced visible-light absorption driven by structural heterogeneity, supported by elevated Urbach energies that indicate substantial disorder beneficial for defect-mediated charge trapping. Photocatalytic evaluations demonstrate outstanding degradation efficiencies 91.98% for Methylene Blue, 88.27% for Crystal Violet, and 47.45% for tetrazine (a 783% improvement over pure ZnO) highlighting strong composition-performance correlations linked to pollutant electronic structures. Biogenic capping using lemon extract confers particle size control, improved dispersion, reduced recombination via surface passivation, and enhanced stability, with the most notable impact observed for Methylene Blue, where a 43% absolute improvement suggests synergistic interactions between citrate ions and the equimolar surface. Mechanistic insights attribute performance optimization to maximized heterojunction interface area, Type-II band alignment promoting charge separation, balanced and sustained reactive oxygen species generation, and extended light absorption into the visible region; these effects are reinforced by stable charge distribution that prevents electron-hole accumulation, increased CdO-induced absorption of longer wavelengths (350-400 nm), and mixed-surface compositions that provide diverse adsorption sites tailored to pollutants with differing electronic features, collectively enabling efficient and sustained photocatalytic degradation.

5.2 Practical Implications

These findings carry significant implications for the development of water treatment technologies. The demonstrated composition-dependent optimization enables rational catalyst

design tailored to specific pollutant classes, wherein electron-rich dyes benefit from ZnO-enriched compositions that enhance hydroxyl radical formation, while electron-deficient compounds are more effectively degraded using CdO-enriched formulations that promote superoxide generation. The integration of sonochemical synthesis with biogenic capping agents provides a cost-effective and environmentally benign production route suitable for scale-up, as room-temperature processing and readily available natural capping agents reduce both energy consumption and environmental burden relative to conventional high-temperature methods. The equimolar composition exhibits broad-spectrum activity across structurally diverse pollutants, indicating its potential utility in treating complex wastewater systems containing multiple contaminants. Furthermore, although long-term stability was not the primary focus of this study, the linear degradation kinetics observed over 165 minutes of irradiation suggest limited catalyst deactivation and imply the feasibility of multiple reuse cycles in practical applications.

5.3 Limitations and Challenges

Despite promising performance, the material presents key limitations, including cadmium toxicity risks requiring stability and recycling strategies, reliance on UV irradiation that limits visible-light applicability, and an incomplete mechanistic understanding that warrants advanced analysis of intermediates. Scale-up may also face challenges related to consistency, aggregation, and cost. However, room-temperature synthesis using natural capping agents lowers energy and environmental impact, the equimolar composition shows broad-spectrum activity suitable for complex wastewater, and linear kinetics over 165 minutes indicate minimal deactivation and good potential for reusability.

5.4 Future Research Directions

This investigation opens numerous avenues for continued research in enhancing visible-light activity through doping, noble-metal deposition, or Z-scheme coupling; developing ternary and quaternary systems to optimize band alignment and reduce cadmium content; and advancing surface engineering using tailored biogenic or synthetic capping agents to improve adsorption, prevent aggregation, and boost reactive species generation. Mechanistic insights can be strengthened through techniques such as EPR, time-resolved spectroscopy, and chromatography-mass spectrometry to clarify degradation pathways. Real-wastewater testing is essential to evaluate performance under complex matrices and variable environmental conditions, while alternative synthesis routes including hydrothermal, microwave-assisted, and

electrochemical methods may yield better-controlled nanostructures. Comprehensive toxicity assessments, including cadmium leaching, ecological impact, and end-of-life recovery, are critical before scale-up. Finally, economic analysis comparing this approach with conventional treatment technologies will help determine commercial feasibility and optimal application domains.

5.5 Conclusion

This research establishes $ZnO_{50\%}$-$CdO_{50\%}$ mixed-oxide nanoparticles as highly effective photocatalysts for organic pollutant degradation through advanced oxidation processes. The equimolar composition provides unique advantages arising from maximized heterojunction interfaces, balanced charge generation, and optimized reactive oxygen species production. Biogenic capping with lemon extract offers environmentally friendly means of enhancing performance through particle size control and surface passivation. The demonstrated composition-dependent performance optimization underscores fundamental principles applicable broadly across semiconductor photocatalysis: matching catalyst electronic structure to specific pollutant characteristics proves essential for achieving maximum efficiency. These findings contribute to the growing body of knowledge guiding rational design of next-generation photocatalytic materials for environmental remediation. While challenges remain particularly regarding cadmium toxicity concerns and visible light activation the exceptional performance achieved suggests that continued optimization along identified research directions could yield practical solutions for persistent water pollution problems. As global demand for clean water intensifies and regulatory standards tighten, advanced photocatalytic technologies will likely play increasingly important roles in water treatment infrastructure. This work provides a solid foundation for continued development toward that goal.

Reference

[1] N. Sahu, R. Duchaniya, Synthesis of ZnO-CdO Nanocomposites, Journal of Materials Science & Surface Engineering, 1 (2013) 11-14.

[2] N.M. Al-Hada, H. Mohamed Kamari, C.A.C. Abdullah, E. Saion, A.H. Shaari, Z.A. Talib, K.A. Matori, Down-top nanofabrication of binary (CdO) x (ZnO) 1–x nanoparticles and their antibacterial activity, International Journal of Nanomedicine, DOI (2017) 8309-8323.

[3] P. Kumar, M.C. Mathpal, G.K. Inwati, S. Ghosh, V. Kumar, W. Roos, H. Swart, Optical and surface properties of Zn doped CdO nanorods and antimicrobial applications, Colloids and Surfaces A: Physicochemical and Engineering Aspects, 605 (2020) 125369.

[4] V.K. Gupta, A. Fakhri, S. Tahami, S. Agarwal, Zn doped CdO nanoparticles: structural, morphological, optical, photocatalytic and anti-bacterial properties, Journal of colloid and interface science, 504 (2017) 164-170.

[5] N. Kati, Controlling of optical band gap of the CdO films by zinc oxide, Mater. Sci, 37 (2019) 136-141.

[6] P. Sharmila, R.M. Sebastain, S. Sagar, E. Mohammed, N.J. Tharayil, Dielectric properties and conductivity of (ZnO/CdO) mixed oxide nanocomposite, Ferroelectrics, 474 (2015) 144-155.

[7] R.M. Mohamed, A.A. Ismail, Doping cadmium oxide into mesoporous zinc oxide matrix for enhanced removal/reduction of Hg (II) Ions, Ceramics International, 47 (2021) 9896-9906.

[8] R. Vinodkumar, K. Lethy, P. Arunkumar, R.R. Krishnan, N.V. Pillai, V.M. Pillai, R. Philip, Effect of cadmium oxide incorporation on the microstructural and optical properties of pulsed laser deposited nanostructured zinc oxide thin films, Materials Chemistry and Physics, 121 (2010) 406-413.

[9] T. Terasako, Y. Ogura, K. Ohmae, S. Fujimoto, M. Yagi, S. Shirakata, Morphological, electrical and optical properties of highly oriented undoped and doped zinc oxide and cadmium oxide films grown by atmospheric-pressure chemical vapor deposition, Surface and Coatings Technology, 230 (2013) 245-253.

[10] K. Sirohi, S. Kumar, V. Singh, N. Chauhan, A. Vohra, Facile synthesis of CdO–ZnO nanocomposites for photocatalytic application in visible light, Arabian Journal for Science and Engineering, 49 (2024) 273-284.

[11] W. Lehmann, Zinc Oxide and Zinc-Cadmium Oxide Phosphors, Journal of the Electrochemical Society, 115 (1968) 538.

[12] R. Saravanan, F. Gracia, M.M. Khan, V. Poornima, V.K. Gupta, V. Narayanan, A. Stephen, ZnO/CdO nanocomposites for textile effluent degradation and electrochemical detection, Journal of molecular liquids, 209 (2015) 374-380.
[13] T.K. Pathak, J.K. Rajput, V. Kumar, L. Purohit, H. Swart, R. Kroon, Transparent conducting ZnO-CdO mixed oxide thin films grown by the sol-gel method, Journal of Colloid and Interface Science, 487 (2017) 378-387.
[14] I.M. Maafa, A.M. Al-Enizi, A. Abutaleb, N.I. Zouli, M. Ubaidullah, S.F. Shaikh, M.A. Al-Abdrabalnabi, A. Yousef, One-pot preparation of CdO/ZnO core/shell nanofibers: An efficient photocatalyst, Alexandria Engineering Journal, 60 (2021) 1819-1826.
[15] H. Ullah, R. Rahaman, S. Mahmud, Optical properties of cadmium oxide (CdO) thin films, Indonesian Journal of Electrical Engineering and Computer Science, 5 (2017) 81-84.
[16] A.S. Kalathur, Cathodic electrodeposition of cadmium oxide, zinc oxide and mixed cadmium oxide-zinc oxide thin films, The University of Texas at Arlington2005.
[17] X. Wu, T. Coutts, W. Mulligan, Properties of transparent conducting oxides formed from CdO and ZnO alloyed with SnO 2 and In 2 O 3, Journal of Vacuum Science & Technology A: Vacuum, Surfaces, and Films, 15 (1997) 1057-1062.
[18] P.S. Kumar, M. Selvakumar, P. Bhagabati, B. Bharathi, S. Karuthapandian, S. Balakumar, CdO/ZnO nanohybrids: facile synthesis and morphologically enhanced photocatalytic performance, Rsc Advances, 4 (2014) 32977-32986.
[19] T. Singh, D. Pandya, R. Singh, Synthesis of cadmium oxide doped ZnO nanostructures using electrochemical deposition, Journal of alloys and compounds, 509 (2011) 5095-5098.
[20] D. Singhwal, A. Khatri, P.S. Rana, Effect of codoping of Zn and Ag on the spatial, optical and photocatalytic properties of cadmium oxide nanoparticles, Optik, 274 (2023) 170562.
[21] A. Ravichandran, A. Robert Xavier, K. Pushpanathan, B. Nagabhushana, R. Chandramohan, Structural and optical properties of Zn doped CdO nanoparticles synthesized by chemical precipitation method, Journal of Materials Science: Materials in Electronics, 27 (2016) 2693-2700.
[22] K. Karthik, S. Dhanuskodi, C. Gobinath, S. Prabukumar, S. Sivaramakrishnan, Multifunctional properties of microwave assisted CdO–NiO–ZnO mixed metal oxide nanocomposite: enhanced photocatalytic and antibacterial activities, Journal of Materials Science: Materials in Electronics, 29 (2018) 5459-5471.
[23] T. Munawar, S. Yasmeen, F. Hussain, K. Mahmood, A. Hussain, M. Asghar, F. Iqbal, Synthesis of novel heterostructured ZnO-CdO-CuO nanocomposite: characterization and

enhanced sunlight driven photocatalytic activity, Materials Chemistry and Physics, 249 (2020) 122983.
[24] P. Labhane, V. Huse, L. Patle, A. Chaudhari, G. Sonawane, Synthesis of Cu doped ZnO nanoparticles: crystallographic, optical, FTIR, morphological and photocatalytic study, Journal of Materials Science and Chemical Engineering, 3 (2015) 39-51.
[25] T. Thangeeswari, A.T. George, A.A. Kumar, Optical properties and FTIR studies of cobalt doped ZnO nanoparticles by simple solution method, Indian J. Sci. Technol, 9 (2016) 1-4.
[26] S. Talam, S.R. Karumuri, N. Gunnam, Synthesis, characterization, and spectroscopic properties of ZnO nanoparticles, International Scholarly Research Notices, 2012 (2012) 372505.
[27] A. Kem, M.R. Ansari, P. Prathap, M. Jayasimhadri, K.R. Peta, Eco-friendly green synthesis of stable ZnO nanoparticles using citrus limon: X-ray diffraction analysis and optical properties, Physica Scripta, 97 (2022) 085814.
[28] R.V. Poonguzhali, E.R. Kumar, M. Sumithra, N. Arunadevi, C.S. Rahale, A.M. Munshi, G.A. Mersal, N.M. El-Metwaly, Natural citric acid (lemon juice) assisted synthesis of ZnO nanostructures: Evaluation of phase composition, morphology, optical and thermal properties, Ceramics International, 47 (2021) 23110-23115.
[29] Q.-r. Feng, J.-d. Guo, X.-l. Xu, H. Zhang, X. Zhu, S.-q. Feng, The effect of ionic radius of metal element (M) on (Pb, M)-1212 superconductors (M= Sr, Ca, Mg, Hg, Cd, Cu), Solid state communications, 94 (1995) 21-25.
[30] S.T. Breviglieri, É.T.G. Cavalheiro, G.O. Chierice, Correlation between ionic radius and thermal decomposition of Fe (II), Co (II), Ni (II), Cu (II) and Zn (II) diethanoldithiocarbamates, Thermochimica acta, 356 (2000) 79-84.
[31] S. Baruah, J. Dutta, Hydrothermal growth of ZnO nanostructures, Science and technology of advanced materials, 10 (2009) 013001.
[32] K. Qi, C. Zhuang, M. Zhang, P. Gholami, A. Khataee, Sonochemical synthesis of photocatalysts and their applications, Journal of Materials Science & Technology, 123 (2022) 243-256.
[33] H. Xu, B.W. Zeiger, K.S. Suslick, Sonochemical synthesis of nanomaterials, Chemical Society Reviews, 42 (2013) 2555-2567.
[34] P. Cintas, J.-L. Luche, Green chemistry. The sonochemical approach, Green Chemistry, 1 (1999) 115-125.

[35] J. Behal, M.S. Maru, R. Katwal, D. Pathak, V. Kumar, Ultrasonic assisted green synthesis approach for nanotechnological materials, Journal of Alloys and Compounds Communications, 3 (2024) 100013.
[36] A.Q. Malik, H. Singh, A. Kumar, R. Aepuru, D. Kumar, Q. ul Ain, A.A. Bhat, A. Mubayi, An Overview on Magnetic Separable Spinel as a Promising Materials for Photocatalysis and Waste Water Treatment, ES Energy & Environment, 19 (2022) 744.
[37] B. Suresh, M. Saravanan, S. Senthil, V. Ratchagar, A. Muthuvel, M. Ayyar, M. Santhamoorthy, N. Azum, Structural, Optical, and Photocatalytic Properties of CdO/La2O3/PVP Nanocomposites by Microwave Irradiation Method, Physics of the Solid State, 67 (2025) 885-894.